Hindawi
Journal of Electrical and Computer Engineering
Volume 2024, Article ID 9790725, 1 page
https://doi.org/10.1155/2024/9790725

Retraction

Retracted: Electronic Controller Automatic Test System Based on Intelligent Control Algorithm

Journal of Electrical and Computer Engineering

Received 23 January 2024; Accepted 23 January 2024; Published 24 January 2024

This article has been retracted by Hindawi following an investigation undertaken by the publisher [1]. This investigation has uncovered evidence of one or more of the following indicators of systematic manipulation of the publication process:

(1) Discrepancies in scope

(2) Discrepancies in the description of the research reported

(3) Discrepancies between the availability of data and the research described

(4) Inappropriate citations

(5) Incoherent, meaningless and/or irrelevant content included in the article

(6) Manipulated or compromised peer review

The presence of these indicators undermines our confidence in the integrity of the article's content and we cannot, therefore, vouch for its reliability. Please note that this notice is intended solely to alert readers that the content of this article is unreliable. We have not investigated whether authors were aware of or involved in the systematic manipulation of the publication process.

Wiley and Hindawi regrets that the usual quality checks did not identify these issues before publication and have since put additional measures in place to safeguard research integrity.

We wish to credit our own Research Integrity and Research Publishing teams and anonymous and named external researchers and research integrity experts for contributing to this investigation.

The corresponding author, as the representative of all authors, has been given the opportunity to register their agreement or disagreement to this retraction. We have kept a record of any response received.

References

[1] M. Li and X. Gong, "Electronic Controller Automatic Test System Based on Intelligent Control Algorithm," *Journal of Electrical and Computer Engineering*, vol. 2022, Article ID 6094612, 13 pages, 2022.

Hindawi
Journal of Electrical and Computer Engineering
Volume 2022, Article ID 6094612, 13 pages
https://doi.org/10.1155/2022/6094612

Research Article

Electronic Controller Automatic Test System Based on Intelligent Control Algorithm

Meiqi Li[1] **and Xu Gong**[2]

[1]*Hubei University of Technology, Wuhan 430070, China*
[2]*Stat Grid Hubei Transmission and Transformation Engineering Co.,Ltd., Wuhan 430070, China*

Correspondence should be addressed to Meiqi Li; 2010221129@hbut.edu.cn

Received 12 April 2022; Accepted 11 May 2022; Published 13 June 2022

Academic Editor: Wei Liu

In order to improve the automatic test effect of the electronic controller, this paper combines the intelligent control algorithm to construct the automatic test system of the electronic controller. Moreover, the paper makes a detailed theoretical analysis of several basic problems relating to signal integrity and gives a general method to solve the main SI problems. In addition, this paper analyzes the principle of the microstrip transmission line parameter model and its relationship with the signal integrity and constructs an automated test system for an intelligent electronic controller. The simulation test results show that the electronic controller automated test system based on the intelligent control algorithm proposed in this paper can play an important role in the electronic controller automated test.

1. Introduction

Automatic test system refers to the general term of the organic whole of test instruments and other equipments combined with a computer as the control core to complete a certain test task under program control. The development of automatic test system has gone through three stages. The first generation of automatic test system adopts logic, timing circuit, or computer to control. Because the bus standard has not yet been determined, the designer needs to design the interface circuit between the controller and the instrument. This interface circuit is generally dedicated, and the versatility is very poor. The second-generation automatic test system solves the bus problem of the test system. The representative ones are the GPIB and CAMAC bus standards that appeared in the 1970s. The appearance of the standard interface bus standardizes the interface of the hardware, but the test software is still not unified. The third generation of automatic test system is marked by the emergence of virtual instrument technology. This concept was first proposed by National Instruments in the 1980s. Virtual instrument technology makes the focus of the whole test system turn to test software, and the large-scale application of virtual instrument technology in the field of automated testing solves the problem of the universality of the test system.

In the automotive industry, with the wide application of electronic technology and computer technology, the automobile has gradually shifted from the original technology of mechanical coordination to the technology of mechatronics, and more and more electronic control units (ECUs) will be used. A car is becoming more and more intelligent, so, to some extent, the electronic technology determines the future development direction of the automobile technology.

At present, the most widely used bus technologies in automobiles include the CAN bus introduced by Bosch and the LIN bus introduced by Volkswagen and Volvo, and the FlexRay bus and MOST bus are also used in automobiles. With the improvement of the transmission rate and the increase of the data transmission bandwidth, the traditional CAN bus is difficult to meet the increase of this demand, so as per the replacement and upgrade of the CAN bus, the CANFD bus has been designed. If the communication behavior of the vehicle bus fails, it will pose a threat to the vehicle network, seriously affect the driving safety of the

vehicle, and bring serious consequences to personal safety. Therefore, it is particularly important to test the electronic components in the vehicle network. There are more and more applications of ECUs in automobiles. The traditional manual testing is inefficient and affects the development cycle of automobiles. Therefore, a complete bus automation test platform is established to replace the inefficient manual testing. Testing efficiency is a common requirement of many OEMs today.

This paper combines the intelligent control algorithm to construct the electronic controller automatic test system, which promotes the improvement of the subsequent electronic controller automatic test effect, and provides a reference for the improvement of the electronic controller automatic control stability.

2. Related Work

Automated testing is a process of converting human testing behavior into machine-executed testing, which can not only effectively save time, manpower, and material resources, but also make testing more efficient [1]. The automated test system is mainly based on computer program control, including the general term for all test instruments and other equipment. With the continuous improvement of the level of science and technology, the functions of automated test systems are also constantly improving after staged development [2]. Embedded automation control system is a controller with industrial control machine as the core with the help of ARM embedded technology, realizing various program control instruments and equipment, bus interface for information exchange and transmission, and test software that accepts and executes test tasks. There are five parts of various devices that need to be tested [3]. The automated test systems cooperate with each other in the process of testing and play a role together to complete the high-efficiency test [4].

The embedded automatic test system of the automotive electronic controller will be able to complete the automatic test of the vehicle's electronic appliances and verify and evaluate it. By setting various environmental tests or condition tests, finding its deficiencies, and conducting effective analysis and rectification, the coordinated work of the various components of the in-vehicle electronic equipment is designed as a complete test system. In the process of test system design and research, attention should also be paid to reducing human participation to the greatest extent, reducing the degree of influence on the test results and ensuring the high efficiency and reliability of the test system [5]. In this test system, the single-module function test and the complete vehicle automation test of the vehicle electronic module can be completed, which are the main two parts of the test system [6].

Although the single-module functional test has examined various data indicators of performance before getting on the vehicle and has met the requirements of on-board electronic equipment, daily dynamic monitoring is still required during the vehicle operation test to detect abnormal data in time and realize hidden danger analysis. Its hardware design consists of three functional modules, including the system power supply module and the display module, with the industrial computer module as the core. Each of these modules has different functions, so the development and design methods are also different [7]. When designing the industrial computer module, pay attention to the selection of the industrial computer. The industrial computer needs to meet the interface requirements of various devices in the network test. It adopts a 4U standard chassis that is easy to install, has a special slot bottom plate in the chassis, and has strong antimagnetic, and shock-proof capabilities [8]. In the design of the system power module, attention should be paid to the realization of its power control function for the entire system, as well as the functions of short-circuit protection and emergency braking. Once overvoltage or overcurrent occurs, immediately use the air switch and circuit breaker to cut off the system power [9]. The system power module is mainly powered by the power control box to the program-controlled power supply on the one hand, and then the program-controlled power supply to the bench and the test board, on the other hand, from the power supply to the test board and then to the ECU. The power supply program control signal is sent to the program control power supply, so as to realize the power supply of the whole system [10]. The power management module is designed to enable the power to be turned on or off independently to prevent sudden power failure and short circuit. UPS uninterruptible power supply can also be used. Usually, the system power supply is charged, and the uninterruptible power supply is used for power supply after power failure. Thirdly, the design of the display module should realize the precise capture, measurement, and analysis of the output characteristics of the CAN signal, so that the control host can support the physical layer test of the CAN network [11].

The development and design of the single-module functional test system software is to use the test software to carry out unified management and statistics of complex operations, which is easy to operate. Its main function is to perform test management, execution, and report generation [12]. In the development and design of test management software, authorization management, simple man-machine dialogue interface, maintenance of vehicle models and test specifications, maintenance of test cases, parameter setting, test fault code storage, and other related operations should be realized [13]. The test execution process should make the test execution interface easy to operate and the steps are concise. After the network management interface is associated with the network database, no manual input is required in the test execution interface, and all nodes of the network can be displayed directly in the drop-down box. After the test report is generated, it can be saved as Excel or XML format. The data files generated during the test are automatically stored in the specified folder and can be opened and viewed [14].

The electronic controllers of vehicle manufacturers vary from about 10 to 30 per vehicle model due to the complexity of the vehicle models. The most common vehicle controllers include engine control units, transmission control units, braking systems, electronic parking, air conditioning, body

control, keyless control, instrumentation, entertainment system, Park Assist, antipinch window control, and sunroof. These controllers are wired to their respective operating switches, sensors, and external motors or actuators [15]. The ports between the wires are designed according to the design requirements of the electrical industry and the electrical characteristics requirements of the automotive electronics industry. Between each controller, there is also a network connection for fast data communication. Common networks such as CAN (controller area network) or LIN (local connection network) realize communication. At the basic protocol level of communication, there are physical layer and design requirements for data links [16]. At present, all electronic controllers are required to realize the diagnosis of electronic controllers that can be diagnosed through external devices. Generally, this diagnosis is mostly based on the existing CAN network. Although the diagnosis specification refers to the main frame of the ISO standard, the detailed design and accessed service support and encryption requirements still need to be designed according to the individual specifications of different OEMs [17].

3. Basic Theory and Basic Problems of Signal Integrity Analysis

For digital signals, one view is that when the trace delay reaches or exceeds 1/5 of the signal rise time t_r, it can be regarded as a high-speed signal, and the transmission line effect needs to be considered. Another view is that the important time-domain characteristics of any digital signal are determined by the spectrum below the signal corner frequency f_{knee} ($f_{\text{knee}} = 0.5/t_r$). As long as the corner frequency of the signal is high enough ($f_{\text{knee}} > 150\,\text{MHz}$), it can be called a high-frequency circuit.

According to the microwave theory, the microstrip transmission line is actually transformed from the two-conductor transmission line, as shown in Figure 1. Its electromagnetic energy is confined or confined between conductors and propagates along the axis of the conductors. The guided traveling waves are TEM waves (transverse electromagnetic waves) or quasi-TEM waves.

When conducting field analysis, it is generally assumed that each electromagnetic variable is time-harmonic to simplify the operation; that is, the time change of the field variable can be expressed by the following expression:

$$F(x, y, z, t) = \text{Re}\left[F(x, y, z)e^{j\omega t}\right]. \tag{1}$$

According to the theory of time-harmonic Maxwell equations, combined with the boundary conditions of the TEM wave, it is assumed that the electromagnetic wave propagates in the form of a plane wave (that is, if the direction of E is defined as x, then $E = a_x E_x(z,t), H = b_y H_y(z,t)$). At the same time, it is assumed that the medium and the conductor are passive and linearly uniform (that is, μ, ε, σ is both linear and isotropic; it does not change with the change of the applied electromagnetic field, $\rho = 0$). According to Gauss's theorem and the equivalence relationship of $D = \varepsilon E$, $\nabla \cdot E = 0$ can be obtained, and then according to the transformation equation $\nabla^2 E = \nabla(\nabla \cdot E) - \nabla \times (\nabla \times E) = -\nabla \times (\nabla \times E)$ to salmon, combined with Faraday's theorem and Ampere's theorem, the wave equation of the time-harmonic plane TEM wave can be deduced as follows:

$$\text{Electricfield wave formula: } \nabla^2 a_x E_x(z,t) - \varepsilon\mu \frac{\partial^2 a_x E_x(z,t)}{\partial t^2} - \mu\sigma \frac{\partial a_x E_x(z,t)}{\partial t} = 0, \tag{2a}$$

$$\text{The field wave formula: } \nabla^2 b_y H_y(z,t) - \mu\varepsilon \frac{\partial^2 b_y H_y(z,t)}{\partial t^2} - \mu\sigma \frac{\partial b_y H_y(z,t)}{\partial t} = 0. \tag{2b}$$

Among them, $\mathbf{a}_x E_x(z,t)$ represents the component in the x direction when $\mathbf{E}(x, y, z, t)$ propagates along the z direction; $\mathbf{b}_y H_y(z,t)$ represents the component in the y-direction of $\mathbf{H}(x, y, z, t)$ as it propagates in the z direction.

According to formula (1), the prototype of $E(x, y, z, t)$ is defined as $\text{Re}[E_x(z)e^{j\omega t}]$, and combined with the definition of vector operator ∇^2, the formula can be obtained

$$\frac{\partial^2 \widehat{E}_x(z)}{\partial z^2} + j\omega\mu(\sigma + j\omega\varepsilon)\widehat{E}_x(z) = 0, \tag{3}$$

$\gamma = \sqrt{j\omega\mu(\sigma + j\omega\varepsilon)} = \alpha + j\beta$ is defined as the propagation constant. It is easy to obtain the general solution of the above formula as

$$E_x(z) = E_m^+ e^{-\gamma z} + E_m^- e^{\gamma z}. \tag{4}$$

The above equation shows that the time-harmonic planar TEM wave only propagates in two directions, the z^+ direction and the z^- direction. The propagation constant γ describes the attenuation and phase shift of the waveform. The real part α of γ describes the loss of the signal through conductors and dielectrics, which is called the loss constant. The imaginary part $\beta = (\omega/v_p) = \omega\sqrt{\mu_0\varepsilon_0}$ is called the phase shift constant, and its magnitude is only related to the frequency and phase velocity of the electromagnetic wave. In TEM waves, E, H, and v are always perpendicular to each other. If it is assumed that the magnetic field direction of the microstrip transmission line is perpendicular to the surface of the conductor, the propagation of the electromagnetic wave in its guidance is shown in Figure 2.

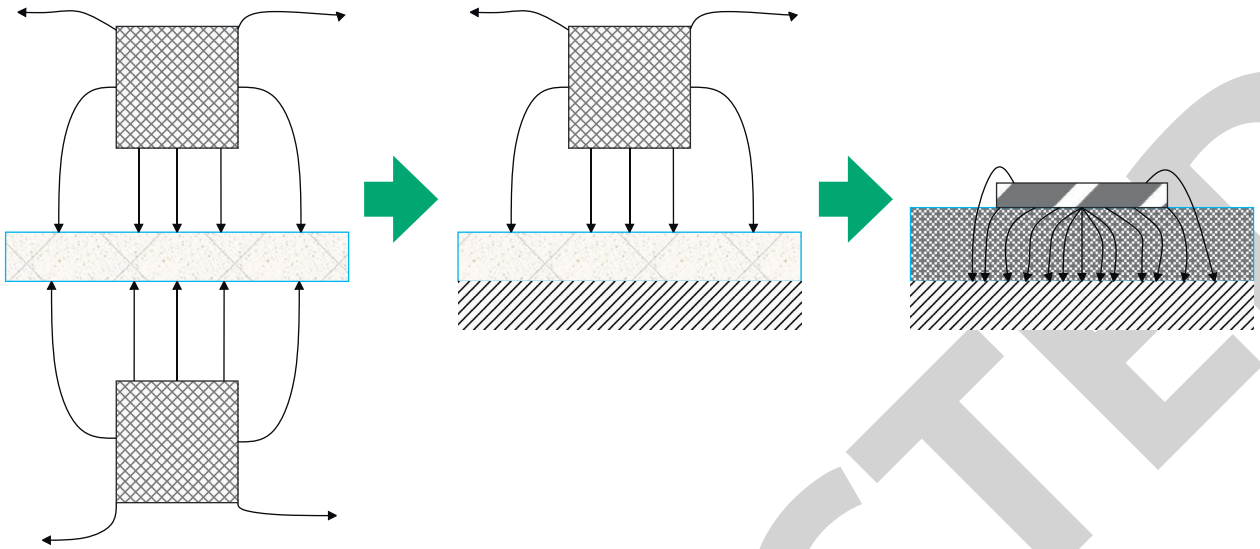

Figure 1: Evolution process of microstrip transmission line.

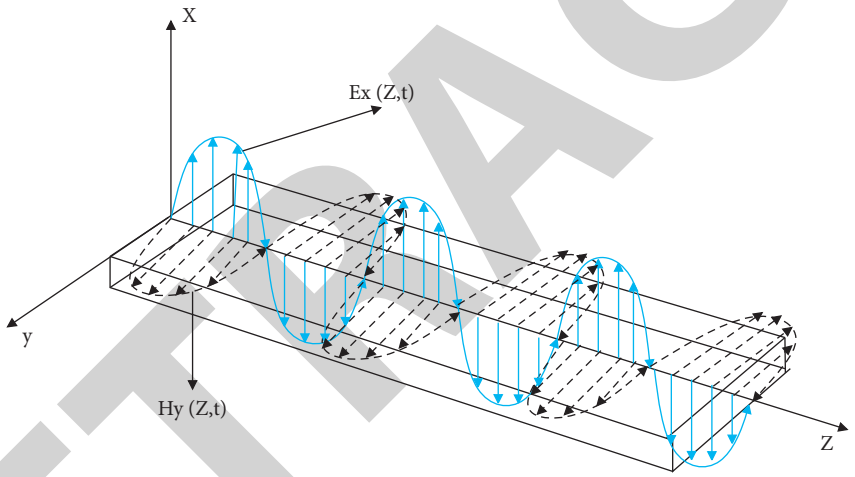

Figure 2: Propagation diagram of harmonic plane wave during TEM of microstrip transmission line.

We note that the conclusions of formulas (2a), (2b), and (4) are only established in very ideal environments (TEM, passive, linear, uniform, and plane wave). In the actual microstrip transmission circuit, there are always various nonideal factors, which lead to the distortion of the signal electromagnetic wave. These undesirable factors include the following.

(1) *The Uneven Change of the Medium*. A typical case is a microstrip line, as shown in Figure 3, because the microstrip line always has a part of the conductor exposed in the air or covered in a protective film and a part in the PCB medium. The surrounding medium is always nonuniform, which leads to the nonuniform change of the surrounding electromagnetic field, resulting in the change of the dielectric constant of the medium and the change of the signal propagation speed. For a microstrip differential trace, as shown in Figure 4, there are more electric field lines in the medium in the even-mode state than in the odd-mode case. That is, the effective dielectric constant of the microstrip differential line in the even-mode case is higher than the odd-mode case. This causes the odd mode of the microstrip differential signal to propagate faster than the even mode, which can cause mode abrupt changes in the signal at the receiver and cause far-end noise.

(2) *Conductor Loss*. Conductor loss is generally divided into two parts: DC loss (copper/iron loss) and AC loss (skin effect). The current of the microstrip line is mainly concentrated near the bottom of the reference plane, and its AC resistance can be obtained as follows:

$$R_{AC} = \sqrt{\frac{\pi \mu f}{\sigma}} \left(\frac{1}{w} + \frac{1}{6h} \right). \tag{5}$$

In the formula, w is the width of the microstrip line, h is the thickness of the medium, and f is the AC frequency of the signal.

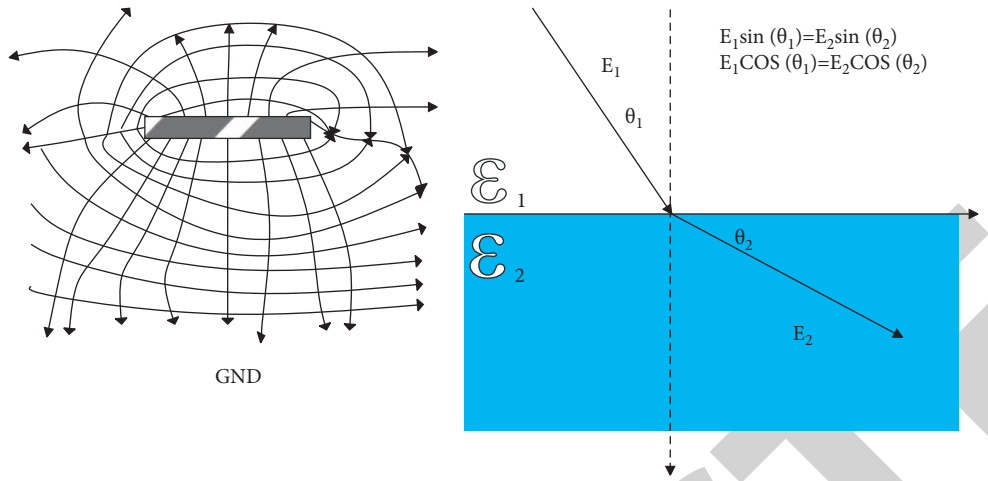

Figure 3: Schematic diagram of the change of the electromagnetic field at the boundary between the microstrip medium and the air. (a) Schematic diagram of the electromagnetic field of the microstrip line. (b) Variation of electric field lines at the boundary of the medium.

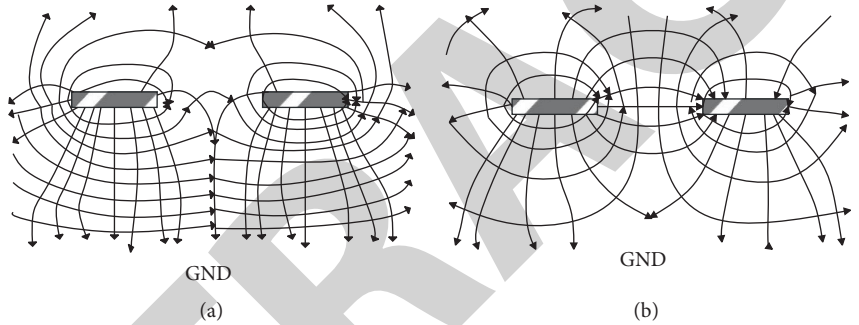

Figure 4: Electromagnetic field distribution in odd-mode and even-mode states of microstrip differential line. (a) Accidental state (++). (b) Odd-mode state (+−).

When the frequency rises to a point where the skin depth is less than the thickness of the conductor, the AC resistance will rise above the DC resistance to dominate and it starts to be proportional to $\sqrt{f}$.

(3) *Frequency, Temperature, and Humidity Effects of the Medium*. For general high-speed circuit design (within 2 GHz), we generally only pay attention to the relative dielectric constant of the medium and the change of the dielectric loss factor with frequency. For the design of higher speed (above 2 GHz), the influence of environmental factors and the interweaving effect of substrate fibers must be considered. The composite permittivity of a lossy dielectric is defined as follows:

$$\varepsilon = \varepsilon' - j\frac{\sigma}{\omega} = \varepsilon' - j\varepsilon''. \tag{6}$$

In the above formula, σ refers to the equivalent conductivity of the medium, which represents the loss caused by the polarization of the dielectric material. The real part ε' represents the dielectric properties of the material, and the imaginary part ε'' represents the loss properties of the dielectric material. In engineering, relative permittivity ε_r and dielectric loss factor (or loss tangent) tan δ are often used to describe the material properties of lossy media. Its relationship with the composite dielectric constant is as follows:

$$\varepsilon_r = \frac{\varepsilon'}{\varepsilon_0}, \tag{7a}$$

$$\tan|\delta| = \frac{\varepsilon''}{\varepsilon'}. \tag{7b}$$

The composite permittivity of such a lossy dielectric can then be expressed as $\varepsilon = \varepsilon_r\varepsilon_0 - j\varepsilon_r\varepsilon_0 \tan\delta$.

If it is assumed that the resistance, inductance, capacitance, and reactance per unit length of a uniform ideal transmission line are R, L, C, and G, respectively. The distributed parameter circuit model of the uniform ideal transmission line can be expressed as the form shown in Figure 5.

One of the segments, Δz, was selected for analysis. According to KVL and KCL, Δz is taken as the limit, and it is easy to obtain the first-order partial differential form of the

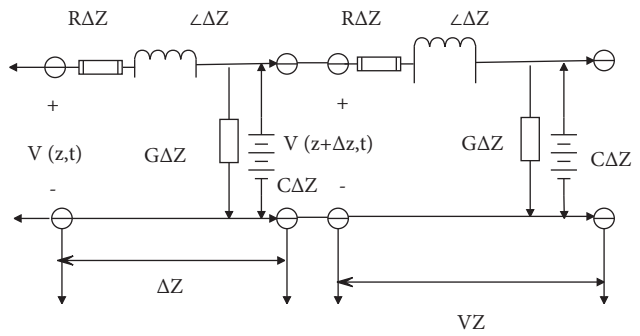

Figure 5: Ideal transmission line distributed parameter circuit model.

uniform transmission line formula (also known as the telegraph formula), which is as follows:

$$\frac{\partial v(z,t)}{\partial z} = -R \cdot i(z,t) - L\frac{\partial i(z,t)}{\partial t}, \tag{8a}$$

$$\frac{\partial i(z,t)}{\partial z} = -G \cdot v(z,t) - C\frac{\partial v(z,t)}{\partial t}. \tag{8b}$$

According to the time-harmonic plane TEM wave characteristics, combined with formula (1), the above formula can be simplified as

$$\frac{\partial V(z)}{\partial z} = -(R + j\omega L) \cdot I(z), \tag{9a}$$

$$\frac{\partial I(z)}{\partial z} = -(G + j\omega C) \cdot V(z). \tag{9b}$$

It is similar to formula (3). It is easy to obtain the propagation constant of the above formula as $\gamma = \sqrt{(R + j\omega L)(G + j\omega C)} = \alpha + j\beta$, and the general solution of the voltage formula in the above formula is

$$V(z) = V_0^+ e^{-\gamma z} + V_0^- e^{\gamma z}. \tag{10}$$

It is similar to the propagation definition of formula (4) for the electric field. In the formula, V^+ represents the voltage propagating forward (z^+ direction), and V represents the voltage propagating backward. Formula (10) is substituted into formula (9a), and the current distribution along the uniform transmission line can be obtained as

$$\begin{aligned} I(z) &= -\frac{1}{R + j\omega L}\frac{\mathrm{d}V(z)}{\mathrm{d}(z)} = \frac{\gamma}{R + j\omega L}\left(V_0^+ e^{-\gamma z} - V_0^- e^{\gamma z}\right) \\ &= \frac{1}{Z_0}\left(V_0^+ e^{-\gamma z} - V_0^- e^{\gamma z}\right). \end{aligned} \tag{11}$$

In the formula, Z_0 is defined as the characteristic impedance of the transmission line:

$$Z_0 = \frac{V_0^+}{I_0^+} = \sqrt{\frac{R + j\omega L}{G + j\omega C}} \underset{R=0,G=0}{\overset{\text{Ideallosslesstransmissionline}}{\rightleftharpoons}} \sqrt{\frac{L}{C}}. \tag{12}$$

As shown in Figure 6, we assume that a unidirectional signal $(V^+(0) = V, V^-(0) = 0)$ starts from $z = 0$ and propagates in the $z+$ direction. In the $t < (l_1/v)$ stage, it can be known from formulas (10) and (11) that the distribution of the voltage on the transmission line along the z direction is $V(z) = V_0 e^{-\gamma z} = I(z)Z_0$. If the transmission line is an ideal lossless transmission line $(R = 0, G = 0)$, the propagation constant is $\gamma = 0 + j\omega\sqrt{LC}$; that is, the amplitude of the signal is not attenuated during propagation, and only the phase changes with z. When there is $t < (l_1/v)$, the impedance suddenly changes to Z_1, and the signal must meet the Maxwell boundary condition at the boundary; that is, the voltage and current at the boundary must be kept unchanged. At this time, the guided wave will be reflected at the boundary, the forward wave will continue to propagate in the $z+$ direction, and the reflected wave will return in the z direction.

According to formulas (10) and (11), the incident wave $[V(l_1^-)^+, I(l_1^-)^+]$ and the reflected wave $[V(l_1^-)^-, I(l_1^-)^-]$ need to satisfy the following equations at the boundary:

$$V(l_1^-)^+ + V(l_1^-)^- = V(l_1^+)^+ = I(l_1^+) \cdot Z_1, \tag{13a}$$

$$I(l_1^-)^+ - I(l_1^-)^- = I(l_1^-)^+. \tag{13b}$$

According to the relationship between the impedance and the voltage and current in formula (12), it can be obtained that the ratio of the reflected voltage to the incident voltage at the boundary $z = l_1$ of the signal is as follows:

$$\frac{V(l_1^-)^-}{V(l_1^-)^+} = \frac{Z_1 - Z_0}{Z_1 + Z_0} = \Gamma. \tag{14}$$

The ratio Γ in the above formula is usually defined as the reflection coefficient. It is substituted into (13a) to obtain the transmitted wave voltage:

$$V(l_1^+)^+ = (1 + \Gamma)V(l_1^-)^+ = \frac{2Z_1}{Z_1 + Z_0}V(l_1^-)^+. \tag{15}$$

As shown in Figure 6, if the impedance R_S of the signal driving end does not match the characteristic impedance Z_0, Z_1 of the transmission line and the load impedance R_L, the signal will be reflected at the impedance change $(z = 0, z = l_1, z = l_2)$. When the reflected signal propagates through the transmission line and encounters the next impedance change, secondary reflection occurs. For the voltage of a specific point A on the trace at a specific time, according to the reflection diagram shown in Figure 6, it can be obtained that in the case of an ideal lossless transmission line, when there is $t = t_A$, the voltage amplitude of point A is [18]

$$V_A(z_A, t_A) = V\left[1 + \Gamma_1 + \Gamma_1\Gamma_S + (1 + \Gamma_1)\Gamma_2(1 - \Gamma_1) + \Gamma_1^2\Gamma_s\right]. \tag{16}$$

Among them, $V = (Z_0/(Z_0 + R_S))E_S$.

With the accumulation of time, the calculation of the voltage at point A or other points will also become more and more complicated. It is not difficult to infer from the above formula that $\Gamma_0 = \Gamma_1 = \Gamma_2 = 0$; namely $R_S = Z_0 = Z_1 = R_L$ must be guaranteed to make the signal at the receiving end

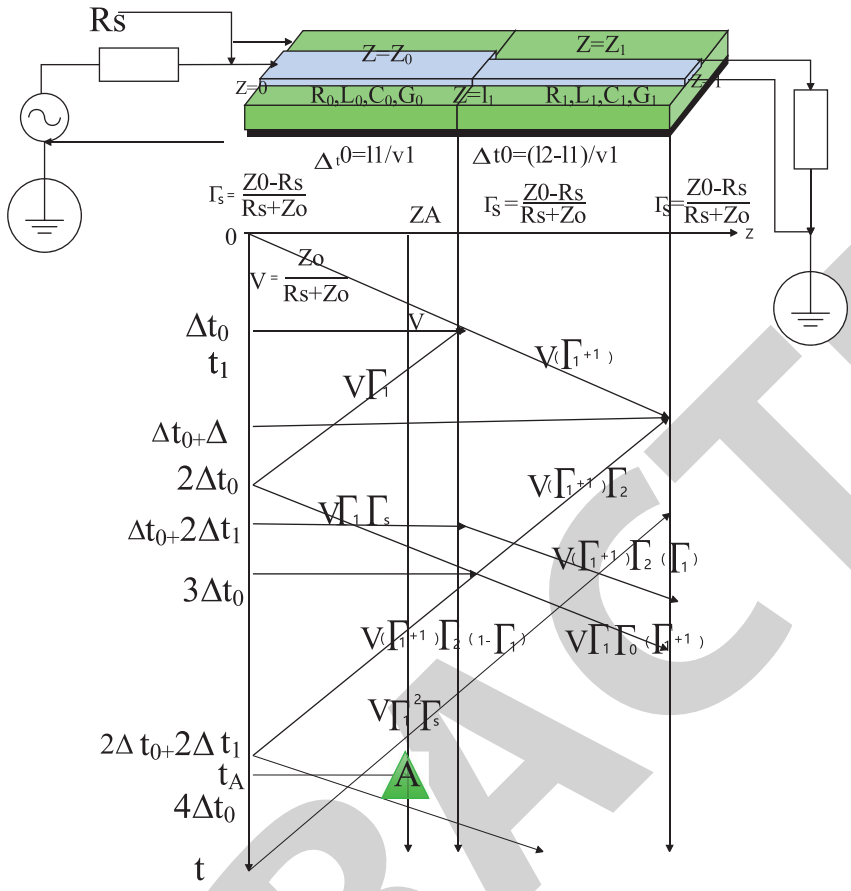

Figure 6: Signal reflection caused by sudden change in impedance of transmission line.

free from ringing and overshoot, which is difficult to achieve in PCB signal transmission.

For capacitive coupling, the total capacitive coupling current in the saturation region is $I_C = C_{12}\Delta x \cdot (\mathrm{d}V/\mathrm{d}t)$.

If it is assumed that the output voltage of the matched driver module is V_1; the corresponding near-end capacitive coupling voltage amplitude V_{NC} and far-end capacitive coupling voltage amplitude V_{FC} are

$$V_{NC} = I_{NC} \cdot Z_0 = \frac{1}{2} \times \frac{1}{2} C_{12} \Delta x \frac{\mathrm{d}V}{\mathrm{d}t} \cdot Z_0 = \frac{1}{4} C_{12} \frac{V_1}{t_r} v t_r \cdot Z_0 = \frac{1}{4} C_{12} v V_1 \cdot Z_0, \tag{17a}$$

$$V_{FC} = I_{FC} \cdot Z_0 = \int \frac{1}{2} C_{12} \frac{\mathrm{d}V}{\mathrm{d}t} \Delta x \cdot Z_0 = \frac{1}{2} C_{12} l_{\mathrm{coup}} \frac{V_1}{t_r} \cdot Z_0. \tag{17b}$$

Among them, C_{12} represents the coupling capacitance per unit length.

v represents the speed of signal propagation (for an ideal lossless transmission line $v = 1/\sqrt{C_{11}L_{11}}, C_{11}, L_{11}$ represents the coupling capacitance per unit length and the coupling inductance per unit length, respectively).

l_{coup} represents the length of the coupling region between the two signal lines.

1/2: the first 1/2 factor in V_{NC} indicates that due to the backward coupling current propagation direction, the signal propagation direction may be opposite, and the equivalent coupling time is $1/2t_r$, $1/2t_r$. The second 1/2 factor indicates that the total coupled inflow is divided into two parts, forward and backward.

For inductive coupling, the total capacitive bare voltage in the saturation region is $V_C = L_{12}\Delta x \cdot (\mathrm{d}I/\mathrm{d}t)$. Similar to capacitive coupling, inductive coupling current will also generate coupling noise at the near and far ends of the transmission line, and its value can be expressed by the following formula [19]:

$$V_{NL} = \frac{1}{2} \times \frac{1}{2} L_{12} v t_r \frac{I}{t_r} = \frac{1}{4} L_{12} v \frac{V_1}{Z_0}, \tag{17c}$$

$$V_{FL} = -\int \frac{1}{2} L_{12} \frac{I}{t_r} \Delta x = -\frac{1}{2} L_{12} \frac{1}{t_r} l_{\text{coup}} \frac{V_1}{Z_0}. \tag{17d}$$

Among them, L_{12} represents the coupled inductance per unit length.

According to the result of formulas (17a)–(17d), it is easy to obtain the superimposed NEXT noise amplitude V_N and FEXT noise amplitude V_F as

$$V_N = V_{NC} + V_{NL} = \frac{1}{4} v \left(C_{12} Z_0 + L_{12} \frac{1}{Z_0} \right) V_1 = \frac{1}{4} \left(\frac{C_{12}}{C_{11}} + \frac{L_{12}}{L_{11}} \right) V_1, \tag{18a}$$

$$V_F = V_{FC} + V_{FL} = \frac{1}{2} \frac{l_{\text{coup}}}{t_r} \left(C_{12} Z_0 - L_{12} \frac{1}{Z_0} \right) V_1 = \frac{1}{2} \frac{l_{\text{coup}}}{t_r} \sqrt{C_{11} L_{11}} \left(\frac{C_{12}}{C_{11}} - \frac{L_{12}}{L_{11}} \right) V_1. \tag{18b}$$

Among them, $v = 1/\sqrt{C_{11} L_{11}}$, $Z_0 = \sqrt{L_{11}/C_{11}}$.

It is not difficult to see from equations (18a) and (18b) that the near-end crosstalk cannot be completely eliminated, while the far-end crosstalk can be completely eliminated under the condition of $C_{12} \cdot L_{11} = C_{11} \cdot L_{12}$. Considering that two single-ended coupled transmission lines can be regarded as a coupled differential pair, the crosstalk coefficient in formulas (18a) and (18b) can be expressed as

$$Kb = \frac{1}{4} \left(\frac{C_{12}}{C_{11}} + \frac{L_{12}}{L_{11}} \right) = \frac{1}{2} \frac{Z_{\text{even}} - Z_{\text{odd}}}{Z_{\text{even}} + Z_{\text{odd}}}, \tag{19a}$$

$$Kf = \frac{1}{2} \sqrt{C_{11} L_{11}} \left(\frac{C_{12}}{C_{11}} - \frac{L_{12}}{L_{11}} \right) = \frac{1}{2} \left(\frac{1}{v_{\text{odd}}} - \frac{1}{v_{\text{even}}} \right). \tag{19b}$$

For a pair of coupled striplines, since the distance between the signal line and the two reference planes is equal and the transmission speed of the odd and even modes is the same, according to (19b), the far-end crosstalk will be 0. However, for a pair of coupled microstrip lines, the odd-mode propagation speed is faster than the even-mode propagation speed, which will result in negative far-end crosstalk at the far end. For coupled microstrip lines, a simple way to calculate the FEXT coefficient is shown in formula (20):

$$Kf \approx k \frac{H^2}{H^2 + D^2}. \tag{20}$$

Among them, k is a constant, H is the distance from the microstrip line to the reference layer, and D is the center distance of the coupled microstrip line. According to formulas (18a), (18b), and (20), it can be inferred that to reduce crosstalk, the most important method is to reduce the length of the parallel wiring (reduce Len), choose a device with low speed (increase t_r), try to take the strip line ($v_{\text{odd}} = v_{\text{even}}$) and the signal is close to the reference layer (reduce H and increase C_{11}), increase the distance between the coupled lines (increase D and decrease C_{12}, L_{12}), keep the reference plane uniform, and complete (reduce impedance mutation).

Before performing timing analysis, it is necessary to understand several important basic timing parameters.

(1) Setup time (t_{setup}) and hold time (t_{hold}): the purpose of timing analysis is to ensure that the setup time margin and hold time margin of the receiver data signal are both greater than 0, as shown in Figure 7(a).

(2) Device valid data output time (t_{co}): for external synchronous or internal synchronous signals, the data bus, address bus, and control bus always lag behind the clock output when outputting externally.

(3) Signal flight time (t_{fly}) 2: as shown in Figure 7(b), the flight time can be divided into the maximum flight time and the minimum flight time according to the different measurement positions.

The maximum flight time refers to the delay time of the signal from the timing measurement level V_{meas} of the driver to the maximum threshold level V_{in} of the logic "0" of the receiver. The minimum flight time refers to the delay time of the signal from the timing measurement level V_{meas} of the driver to the minimum threshold level V_{inh} of the logic "1" at the receiving end. The above level values can be found in the device IBIS model file.

(4) Clock skew (Skew) and jitter (Jitter): for timing analysis, it is mainly divided into two categories: CPU read data and write data. Taking the CPU read and write RAM timing analysis based on internal synchronization as an example, the read and write RAM timing needs to satisfy the following timing inequality:

$$t_{clk} + t_{cll-fly} - t_{co-\text{CPU}} - t_{\text{data}-fly} - t_{RAM-E} = t_{\text{RAM-setup-margin}} > 0, \tag{21a}$$

$$t_{\text{data}-fly} + t_{co-\text{DSP}} - t_{clk-fly} - t_{\text{RAM-hold-min}} = t_{\text{RAM-hold-margin}} > 0, \tag{21b}$$

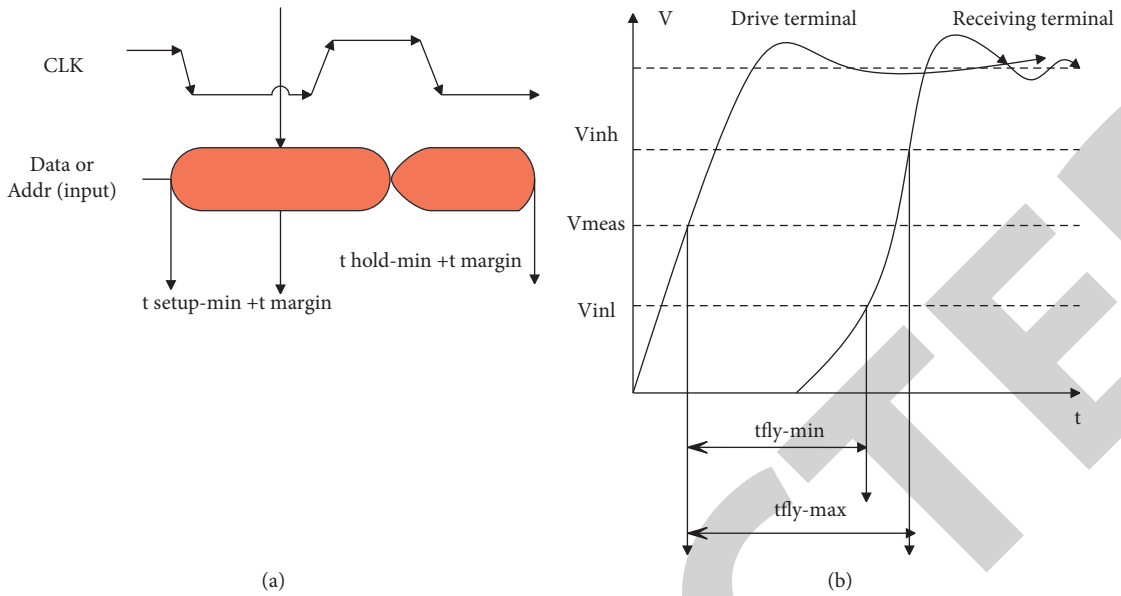

Figure 7: Schematic diagram of several important timing parameters. (a) Setup time and hold time. (b) Maximum and minimum flight time.

$$t_{clk} - t_{clk-fly} - t_{co-\mathrm{RAM}} - t_{\mathrm{data}-flybk} - t_{\mathrm{CPU-setup-min}} = t_{\mathrm{CPU-setup-margin}} > 0, \tag{22a}$$

$$t_{\mathrm{data}-flybk} + t_{co-\mathrm{RAM}} + t_{clk-fly} - t_{\mathrm{CPU-hold-min}} = t_{\mathrm{CPU-hold-margin}} > 0. \tag{22b}$$

Among them, formulas (21a) and (21b) represent the CPU read RAM timing requirement, and formulas (22a) and (22b) represent the CPU read RAM timing requirement.

Jitter can be defined as follows: a signal that is considered to be wandering at a particular moment relative to its ideal time shift.

The jitter J is related to the phase noise $\Delta\varphi$ as follows:

$$J = \frac{1}{2\pi}\Delta\varphi. \tag{23}$$

Therefore, the change in jitter is proportional to the change in phase, and the rate of change $(\mathrm{d}J/\mathrm{d}t)$ of the jitter appears as frequency noise. In general, jitter components can be classified as shown in Figure 8.

Theoretically, the S parameter is defined as the ratio of the power scattering coefficient between ports, but in practical engineering, each port is usually designed to have the same impedance R (usually 50Ω), so the definition of the S parameter of the same impedance port is

$$S_{ij} = \frac{b_i}{a_j} = \frac{\sqrt{P_{i,\mathrm{output}}}}{\sqrt{P_{j,\mathrm{input}}}} = \frac{v_i(z)^-/\sqrt{R}}{v_j(z)^+/\sqrt{R}} = \frac{v_i(z)^-}{v_j(z)^+}. \tag{24}$$

Among them, a_j, b_i represents the square root of the power flowing into network port j and outgoing network port i, respectively, which is called the scattering coefficient; $v_i(z)^-$ represents the back-propagating voltage of port i (port output voltage); $v_j(z)^+$ represents the forward propagating voltage (port input voltage) of port j.

Since there is only one port, the single-ended S parameter can only represent the reflection of the signal.

Generally speaking, the dual-port S parameter is used more, as shown in Figure 9; it includes four quantities: S_{11}, S_{12}, S_{21}, and S_{22}. Among them, S_{11} or S_{22} is also commonly referred to as return loss, and S_{21} is referred to as insertion loss. For an ideal microstrip transmission line system, S_{11} and S_{21} can be expressed as follows:

$$S_{11} = \left|\frac{b_1}{a_1}\right|_{a_2=0} = \frac{v_1^-/\sqrt{R}}{v_1^+/\sqrt{R}} = \frac{v_1^-}{v_1^+} = \Gamma_0 = \frac{Z_{in} - R}{Z_{in} + R}. \tag{25a}$$

$$S_{21} = \left|\frac{b_2}{a_1}\right|_{a_2=0} = \frac{v_2^-/\sqrt{R}}{v_1^+/\sqrt{R}} = \frac{v_2^-}{v_1^+}. \tag{25b}$$

Among them, R is the output impedance of the signal source at port 1, and Z_{in} is the input impedance seen from port 1.

It can be seen from (25a) that S11 represents the reflection of the signal, which is consistent with the reflection of the transmission line in signal integrity. If the peak-to-peak value (or valley value) of the signal S parameter is represented by Δf, it has the following relationship with the signal propagation delay τ_d:

$$\Delta f = \frac{1}{2\tau_d}. \tag{26}$$

The relationship between the dielectric loss factor of the material and the drop-in loss is as follows:

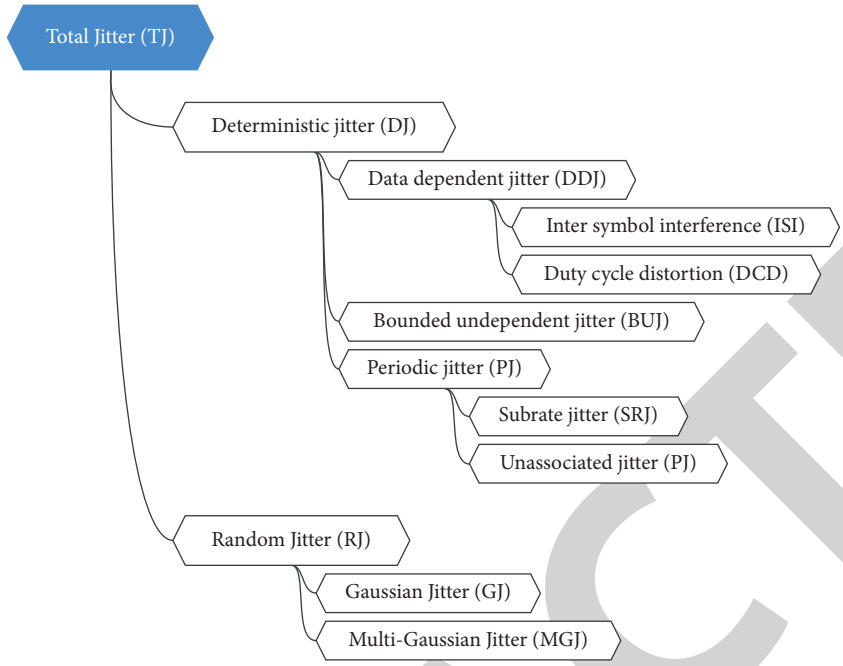

Figure 8: Schematic diagram of classification of jitter.

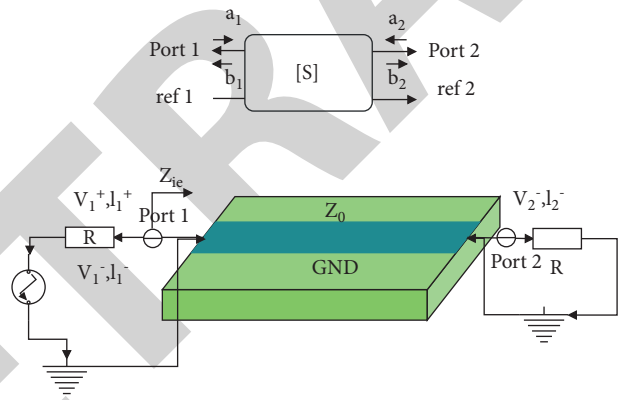

Figure 9: Schematic diagram of two-port S-parameter model of PCB traces.

$$\tan\delta = \frac{-S21\,[\mathrm{dB}]}{2.3 \times \sqrt{\varepsilon} \times \mathrm{Len} \times f}. \tag{27}$$

Among them, tan δ is the dielectric loss factor (or called loss tangent), S21 is the insertion loss (dB), ε is the dielectric constant of the PCB medium, Len is the trace length (in), and f is the frequency (GHz)

4. Electronic Controller Automatic Test System Based on Intelligent Control Algorithm

In this paper, the function automation test of the instrument of the newly developed model is carried out. The instrument mainly has four types of display functions: indication, alarm, information, and setting. This paper verifies whether the design of the instrument meets the requirements of the relevant standards and the design task book through the functional test of the instrument. The interface schematic diagram of the instrument to be tested is shown in Figure 10.

In this paper, the effect of the above model is verified, and the automatic test effect of the intelligent control algorithm in this paper is studied. Moreover, in this paper, the simulation test is carried out through MATLAB, the data statistical analysis is carried out in combination with the intelligent control algorithm, and the experimental test data (test effect evaluation) in Table 1 are finally obtained.

It can be seen from the above simulation experiments that the electronic controller automatic test system based on the intelligent control algorithm proposed in this paper can play an important role in the electronic controller automatic test.

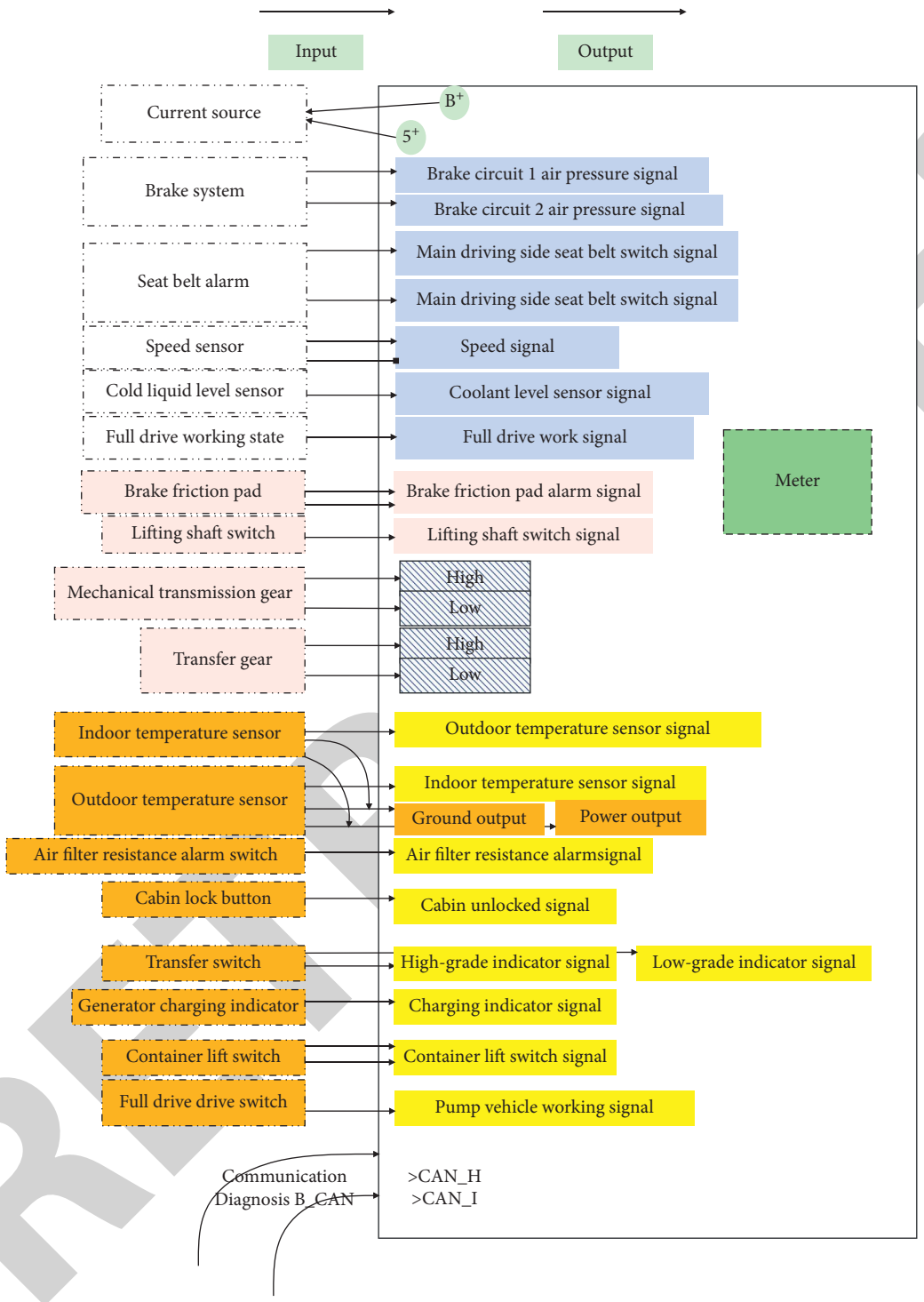

Figure 10: Schematic diagram of instrument interface.

Table 1: Automatic test system of electronic controller based on intelligent control algorithm.

Number	Test effect	Number	Test effect	Number	Test effect
1	81.57	18	73.48	35	70.46
2	80.54	19	74.92	36	82.86
3	69.37	20	81.47	37	83.95
4	81.78	21	74.11	38	80.88
5	83.49	22	78.39	39	74.99
6	68.60	23	73.62	40	81.02
7	78.65	24	71.12	41	67.09
8	80.68	25	73.10	42	75.76
9	83.87	26	83.54	43	83.32
10	69.05	27	79.71	44	74.06
11	83.62	28	70.72	45	79.56
12	75.55	29	73.40	46	68.19
13	77.84	30	82.29	47	83.81
14	72.30	31	79.64	48	80.97
15	73.46	32	82.89	49	68.19
16	82.89	33	79.52	50	82.69
17	78.45	34	70.34	51	76.79

5. Conclusion

The traditional electrical control system adopts a centralized control method, which cannot keep up with the development rhythm of modern automobiles due to the disadvantages of too complicated wiring, high cost, and too low efficiency. There are many electronic control components in modern automobiles, the functions are relatively complex, and the data exchanges among them are very frequent. In order to solve this series of problems, the control method of the electrical system has been distributed in a distributed way, and a new type of bus technology has been produced. The ability of information transmission and error handling among various electronic control elements in the vehicle network is very important to the overall control of the vehicle. This paper combines the intelligent control algorithm to construct the electronic controller automatic test system, which promotes the improvement of the subsequent electronic controller automatic test effect. The simulation test study shows that the electronic controller automatic test system based on the intelligent control algorithm proposed in this paper can play an important role in the electronic controller automatic test.

Data Availability

The labeled dataset used to support the findings of this study are available from the corresponding author upon request.

Conflicts of Interest

The authors declare no conflicts of interests.

Acknowledgments

This study was sponsored by Hubei University of Technology.

References

[1] V. Syrotiuk, S. Syrotyuk, V. Ptashnyk et al., "A hybrid system with intelligent control for the processes of resource and energy supply of a greenhouse complex with application of energy renewable sources," *Przeglad Elektrotechniczny*, vol. 96, no. 7, pp. 149–152, 2020.

[2] L. Vladareanu, V. Vladareanu, H. Yu, D. Mitroi, and A. C. Ciocirlan, "Intelligent control interfaces using extenics multidimensional theory applied on VIPRO platforms for developing the IT INDUSTRY 4.0 concept," *IFAC-PapersOnLine*, vol. 52, no. 13, pp. 922–927, 2019.

[3] P. Zheng, J. Zhang, H. Liu, J. Bao, Q. Xie, and X. Teng, "A wireless intelligent thermal control and management system for piglet in large-scale pig farms," *Information Processing in Agriculture*, vol. 8, no. 2, pp. 341–349, 2021.

[4] M. Nadafzadeh and S. Abdanan Mehdizadeh, "Design and fabrication of an intelligent control system for determination of watering time for turfgrass plant using computer vision system and artificial neural network," *Precision Agriculture*, vol. 20, no. 5, pp. 857–879, 2019.

[5] A. P. Araújo Neto, G. W. Farias Neto, T. G. Neves, W. B. Ramos, K. D. Brito, and R. P. Brito, "Changing product specification in extractive distillation process using intelligent control system," *Neural Computing & Applications*, vol. 32, no. 17, pp. 13255–13266, 2020.

[6] Y. Arya, "Automatic generation control of two-area electrical power systems via optimal fuzzy classical controller," *Journal of the Franklin Institute*, vol. 355, no. 5, pp. 2662–2688, 2018.

[7] N. Harrabi, M. Souissi, A. Aitouche, and M. Chaabane, "Intelligent control of grid-connected AC–DC–AC converters for a WECS based on T–S fuzzy interconnected systems modelling," *IET Power Electronics*, vol. 11, no. 9, pp. 1507–1518, 2018.

[8] H. Yang, A. Alphones, Z. Xiong, D. Niyato, J. Zhao, and K. Wu, "Artificial-intelligence-enabled intelligent 6G networks," *IEEE Network*, vol. 34, no. 6, pp. 272–280, 2020.

[9] M. Al-Khafajiy, S. Otoum, T. Baker et al., "Intelligent control and security of fog resources in healthcare systems via a cognitive fog model," *ACM Transactions on Internet Technology*, vol. 21, no. 3, pp. 1–23, 2021.

[10] L. Haibo, L. Zhenglin, and L. Guoliang, "Neural network prediction model to achieve intelligent control of unbalanced drilling's underpressure value," *Multimedia Tools and Applications*, vol. 78, no. 21, pp. 29823–29851, 2019.

[11] L. Peng and Z. Jiang, "Intelligent automatic pig feeding system based on PLC," *Revista Científica de la Facultad de Ciencias Veterinarias*, vol. 30, no. 5, pp. 2479–2490, 2020.

[12] S. Anila, B. Saranya, G. Kiruthikamani, and P. Devi, "Intelligent system for automatic railway gate controlling and obstacle detection," *International Journal Of Current Engineering And Scientific Research (IJCESR)*, vol. 4, no. 8, pp. 2394–0697, 2017.

[13] L. B. Prasad, H. O. Gupta, and B. Tyagi, "Intelligent control of nonlinear inverted pendulum system using Mamdani and TSK fuzzy inference systems: a performance analysis without and with disturbance input," *International Journal of Intelligent Systems Design and Computing*, vol. 2, no. 3/4, pp. 313–334, 2018.

[14] J. Yang, P. Wang, W. Yuan, Y. Ju, W. Han, and J. Zhao, "Automatic generation of optimal road trajectory for the rescue vehicle in case of emergency on mountain freeway using reinforcement learning approach," *IET Intelligent Transport Systems*, vol. 15, no. 9, pp. 1142–1152, 2021.

[15] X. Yao, J. H. Park, H. Dong, L. Guo, and X. Lin, "Robust adaptive nonsingular terminal sliding mode control for automatic train operation," *IEEE Transactions on Systems, Man, and Cybernetics: Systems*, vol. 49, no. 12, pp. 2406–2415, 2019.

[16] M. J. Mahmoodabadi and M. Taherkhorsandi, "Intelligent control of biped robots: optimal fuzzy tracking control via multi-objective particle swarm optimization and genetic algorithms," *AUT Journal of Mechanical Engineering*, vol. 4, no. 2, pp. 183–192, 2020.

[17] W. He, Z. Li, and C. L. P. Chen, "A survey of human-centered intelligent robots: issues and challenges," *IEEE/CAA Journal of Automatica Sinica*, vol. 4, no. 4, pp. 602–609, 2017.

[18] Y. Huang, S. Liu, C. Zhang, X. You, and H Wu, "True-data testbed for 5G/B5G intelligent network," *Intelligent and Converged Networks*, vol. 2, no. 2, pp. 133–149, 2021.

[19] H. Dong, C. Roberts, Z. Lin, and F. Y Wang, "Guest editorial introduction to the special issue on intelligent rail transportation," *IEEE Transactions on Intelligent Transportation Systems*, vol. 20, no. 7, pp. 2677–2680, 2019.